# Hydrogen Tunneling in an Enzyme Active Site: A Quantum Wavepacket Dynamical Perspective

**3 AUTHORS**, INCLUDING:

Jacek Jakowski
University of Tennessee
**38** PUBLICATIONS **470** CITATIONS

# Hydrogen Tunneling in an Enzyme Active Site: A Quantum Wavepacket Dynamical Perspective

## Srinivasan S. Iyengar,* Isaiah Sumner, and Jacek Jakowski

*Department of Chemistry and Department of Physics, Indiana University, 800 E. Kirkwood Ave, Bloomington, Indiana 47405*

We study the hydrogen tunneling problem in a model system that represents the active site of the biological enzyme, soybean lipoxygenase-1. Toward this, we utilize quantum wavepacket dynamics performed on potential surfaces obtained by using hybrid density functional theory under the influence of a dynamical active site. The kinetic isotope effect is computed by using the transmission amplitude of the wavepacket, and the experimental value is reproduced. By computing the hydrogen nuclear orbitals (eigenstates) along the reaction coordinate, we note that tunneling for both hydrogen and deuterium occurs through the existence of distorted, spherical s-type proton wave functions and p-type polarized proton wave functions for transfer along the donor−acceptor axis. In addition, there is also a significant population transfer through distorted p-type proton wave functions directed perpendicular to the donor−acceptor axis (via intervening $\pi$-type proton eigenstate interactions) which underlines the three-dimensional nature of the tunneling process. The quantum dynamical evolution indicates a significant contribution from tunneling processes both along the donor−acceptor axis and along directions perpendicular to the donor−acceptor axis. Furthermore, the tunneling process is facilitated by the occurrence of curve crossings and avoided crossings along the proton eigenstate adiabats.

## I. Introduction

Hydrogen tunneling has been noted to have a significant effect in many organic reactions[1] and in biological enzyme[2–11] kinetics. Experimental evidence that indicate quantum nuclear and/or tunneling effects are as follows. (a) There is an unexpectedly large primary kinetic isotope effect (KIE), as has been noted for many lipoxygenases. For example, in soybean lipoxygenase-1 (SLO-1),[7,9,10,12–18] the room-temperature rate constant for proton transfer ($k_H$) catalyzed by SLO-1 is nearly a factor of 80 larger than that for deuteron transfer ($k_D$).[13] Human lipoxygenase was noted to have a similar behavior.[19] Quantum mechanical tunneling is believed to be the fundamental reason behind this phenomenon.[7,12,16] (b) In some cases, a weak temperature dependence of the rate constant is seen in conjunction with large primary KIE.[20] (c) An elevated value for the Swain−Schaad exponent[21] [$\log(k_H/k_D)/\log(k_D/k_T)$] has also been noted. (d) Another rather sensitive measure of quantum nuclear effects in enzyme reactions is the presence of secondary KIEs. A well-studied family of examples where secondary KIEs play an important role are the alcohol dehydrogenases, which catalyze the conversion of alcohols to aldehydes or ketones.[2] Because these observations cannot be explained by using standard Arrhenius-type methodologies, many groups have invoked quantum mechanical tunneling models.[4,7,8,11]

A few of the most powerful approaches that attempt to solve the important problem of hydrogen tunneling in biological enzymes are as follows. Truhlar and co-workers[11,21] have utilized a multidimensional tunneling correction to variational transition-state theory,[11,22] where the potential-energy surface calculations are generally obtained from QM/MM techniques.[23] Hammes-Schiffer and co-workers[4,12,24] utilize a vibronically nonadiabatic

formalism that includes quantum mechanical contributions from active electrons and protons that undergo transfer during the proton-coupled electron transfer in SLO-1. The nonadiabatic rate expression[12] includes hydrogen and deuterium ground and excited nuclear wave functions, constructed on the basis of one-dimensional Morse oscillator approximations, and the rate is computed through the product of an electronic coupling and a temperature-dependent term that attenuates the nuclear wave-function overlap.[12] The full protein is explicitly treated through classical molecular dynamics simulations modified by empirical valence-bond[25–28] force-field corrections. Hammes-Schiffer and co-workers have also employed mixed quantum/classical dynamics to study hydrogen tunneling problems.[29] Warshel and co-workers[7,17,30] have utilized centroid molecular dynamics[31,32] on surfaces computed from empirical valence-bond theory.[25–28] Schwartz and co-workers[8] utilize a semiclassical description based on the Langevin equation. A classical dynamics simulation with a Hamiltonian that includes parametrized, analytical potentials and interactions with the environment is conducted to find a friction kernel, which is used to calculate the quantum mechanical rate constant by using the flux operator formalism.[33] Siebrand and Smedarchina[18] used time-dependent perturbation theory, where the quantum potential is a one-dimensional analytical potential. Finally, Klinman and co-workers[2] compute rates with a vibrationally nonadiabatic methodology[34] that employs Franck−Condon-like overlaps.

On the basis of the currently accepted picture of hydrogen transfer, the quantum mechanical potential-energy surface of the transferring nucleus (hydrogen or its heavier isotopes) is initially characterized by a deep well, and corresponding localization of the hydrogen nucleus, on the donor side. As the donor−acceptor distance decreases through gating motions, which may be facilitated by large-scale rearrangements of the protein, the hydrogen atom starts to perceive a stable minimum

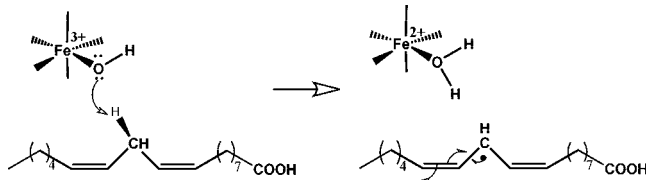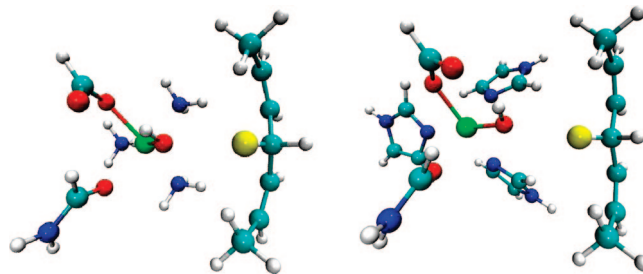* Corresponding author. E-mail: iyengar@indiana.edu.

**Figure 1.** Hydrogen abstraction is the rate-determining step in the oxidation of linoleic acid by SLO-1.



(a) Structure I     (b) Structure II

**Figure 2.** The larger model system (structure II) has a reaction coordinate that is in good agreement with the smaller structure I. (Benchmark calculations are provided in the Appendix.) Hence, structure I and its potential-energy surfaces were utilized for all quantum dynamical calculations. The transferring hydrogen is enlarged and highlighted in yellow.

on the acceptor side. That is, the hydrogen potential surface may start to acquire a double-well character. At this stage, the donor and acceptor moieties may be close to hydrogen-bonding distance, and tunneling can occur. Whether tunneling occurs at this stage depends on many factors including (a) the barrier height, curvature (including higher-order anharmonic contributions that arise from the inherent double-well nature of the problem and may in general be significant), and width along the donor−acceptor and orthogonal directions and (b) the slope and curvature of the potential surface in the region close to the classical turning point, which is generally where tunneling begins. Thus, the nature of the quantum mechanical potential energy surface has a critical bearing on the tunneling process. The situation is further complicated by the probability of multiple transfer paths where the probability of transfer through each path is driven by canonical path sampling.[35,36] In this publication, we undertake a detailed analysis of the role of the quantum mechanical potential surface on the hydrogen nuclear tunneling process involved in a model system that is constructed by using the active-site atoms in close proximity to the iron cofactor in SLO-1. Our approach differs from previous efforts[7,12,16,17] on SLO-1 through the utilization of a quantum wavepacket description[37–40] of the tunneling hydrogen nucleus (proton or deuteron) that is coupled to the change in electronic structure and geometry of the surrounding atoms, both of which are computed by using density functional theory. The computational expense in our calculation is controlled by utilizing only active-site atoms that are in close proximity to the iron cofactor in SLO-1.

SLO-1 is a nonheme metalloenzyme that catalyzes the oxidation of linoleic acid.[7,15–18,41–45] In mammals, lipoxygenase catalyzes the production of leukotrienes and lipoxin and plays an important role in inflammatory responses.[46,47] It has been shown that inhibition of this enzyme inhibits tumor genesis, and lipoxygenase has been proposed as a promising cancer chemopreventive agent.[46,47] The rate-determining step in the catalytic cycle is the abstraction of a hydrogen atom from the fatty acid chain by the octahedral $Fe^{3+}$−OH active-site complex (see Figure 1). This is followed by a radical attack by $O_2$ that results in the final peroxide complex. The rate-determining step displays a large primary KIE ($k_H/k_D = 81$) and also displays a weak temperature dependence of the reaction rate constant.[13] In our study, the transferring hydrogen nucleus (proton or deuteron) in SLO-1 is treated as a three-dimensional quantum wavepacket that is propagated by using an efficient distributed approximating functional (DAF) propagator.[37,38,48,49] At each step of the quantum dynamics, the potential surface is computed by including all electrons in our model system through density functional theory calculations. We find that the dimensionality of the wavepacket is critical. A full three-dimensional description of the wavepacket and associated hydrogen nuclear potential surface is necessary for a quantitative description of the tunneling problem.

The paper is organized as follows. In Section II, we outline the methodological aspects and also introduce our model system.

In Section III, we discuss the quantum dynamical propagation of the tunneling proton and deuteron. Particularly, in Section III.A, we discuss the implications of the potential-energy surface experienced by the tunneling atoms and the corresponding shapes of the nuclear eigenstates (orbitals). These eigenstates and the associated curve crossings and avoided crossings have an important role on the nature of hydrogen and deuterium tunneling in our model system. In Section III.B, we discuss the computation of transmission coefficients of hydrogen and deuterium and relate these to the experimentally observed KIE. In Section IV, we give our conclusions. An appendix is provided to briefly discuss the effect of model system size on accuracy and the choice of electronic structure methods for computing the quantum dynamical potential. In line with others in the literature,[11] we have chosen to refer to proton, hydrogen, and hydride transfer reactions, as well as to those involving heavier isotopes, with the same terminology, that is, hydrogen transfer. Also, when the transferring atom is hydrogen or hydride, we do not need to make any methodological distinctions between the electron traveling with the hydrogen nucleus or separately for reasons that will become apparent.

## II. Computational Details

The rate-determining step in the catalytic cycle is the abstraction of a hydrogen atom from the fatty acid (linoleic acid) chain by the octahedral $Fe^{3+}$−OH complex present deep in the active site (Figure 1). Our approach is to treat this step by using quantum wavepacket dynamics[37] of the hydrogen undergoing transfer, facilitated by ab initio molecular dynamics (AIMD)[50] and electronic structure optimization and frequency calculations.

As noted in the Introduction, the hydrogen-transfer step is facilitated by gating motions of the donor and acceptor moieties. These may be further facilitated by large-scale rearrangements of the protein. Because the main goal of the current publication is to evaluate the quantum nuclear component through rigorous quantum dynamical treatment, conducted on surfaces created from electronic structure, the exact nature of these modes is not explicitly considered here. Thus, we have only considered reduced active-site model systems (see Figure 2). Similar models have been utilized in previous studies on metalloenzymes.[15,51] In our study of both structures in Figure 2, we have included a truncated representation of the substrate to allow radical delocalization upon stripping the hydrogen. Upon inspection of Figure 1, it is clear that the radical remaining in linoleic acid, after hydrogen abstraction, is stabilized by the two $\pi$-bonds present on either side. We have included these unsaturated
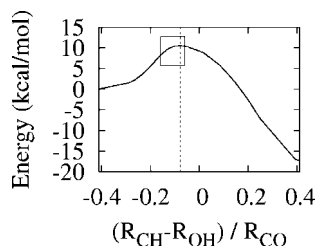
**Figure 3.** The minimum-energy reaction profile for the rate-determining hydrogen abstraction step is shown, and the critical tunneling region is highlighted within a box.

groups in our substrate model for both structure I and II. Structure I is utilized for all of the quantum dynamics results discussed in this paper. It contains a pruned representation of the amino acid ligands binding to the central iron atom in addition to a portion of the substrate. Because the hydrogen tunneling process is a proton-coupled electron-transfer process where the electron transfer has been previously noted to be directed toward the metal center, the properties of the ligands binding to Fe should be suitably modeled. The representation of the ligands in structure I was found to yield suitable energetics along the reaction coordinate (to be defined later) in comparison to the larger model structure II. The average energetic deviation for the hydrogen abstraction reaction along the minimum-energy path between the two structures is about 0.5 kcal/mol, and the average deviation in geometry along the reaction profile is about 0.02 Å. (See the Appendix for details.) An important assumption in the choice of these model systems is that the hydrogen tunneling process is local and mostly influenced by the electronic structure from neighboring groups. Further implications of this reduced model treatment are discussed later in the text and in the conclusions.

**A. Computing a Classical Reaction Path.** For the next step in our procedure, we obtain an approximate classical reaction path corresponding to the transfer of the hydrogen atom from donor to acceptor. This path is utilized later for constructing the hydrogen and deuterium nuclear potential surfaces for quantum dynamics. There exists a number of powerful techniques available in the literature to compute classical reaction paths and to simulate infrequent events.[35,52–55] In our study, a reaction path for the transfer process is obtained by using two independent techniques to confirm results. The final result from both techniques is the minimum-energy path for the shared hydrogen shown in Figure 3, where the horizontal axis represents a reduced reaction coordinate computed from the positions of donor, acceptor, and shared proton, and the vertical axis represents the corresponding electronic-structure energy. It is however important to note that at each point on the horizontal axis, all atoms in the active-site model change coordinates, and the use of a simplified reaction coordinate is only an approximation. In the following two paragraphs, we briefly outline the two techniques we have used to independently confirm Figure 3.

In one case, we have performed relaxed-scan optimization calculations[55] where at each step, the acceptor–proton distance is held fixed, and all other active-site atoms are allowed to relax freely to minimize the energy of the system through a local minimization process available in standard electronic structure packages.[56] Starting from the reactant geometry, the acceptor–proton distance is then incremented in steps of 0.1 Å before and after the critical tunneling region and ≤0.01 Å in the critical tunneling region, where the critical tunneling region is in the range of reaction coordinates [−0.204, −0.0586] as shown in

Figure 3 (this aspect is discussed further below and also later in the text). At each step, a constrained local minimization is performed. The incremental steps span the region between reactant geometry and the product geometry. This way, a potential-energy surface is obtained as a function of different constrained values along the horizontal axis in Figure 3. The calculations are performed by using the B3LYP/lanl2dz level of theory for all electrons in our model structure I. (A similar set of calculations using MP2, discussed in the Appendix, showed good qualitative agreement.)

The surface is then independently confirmed through a second calculation that utilized the AIMD technique, atom-centered density matrix propagation (ADMP)[50,57–61] along with the B3LYP/lanl2dz level of theory for all electrons in our model structure I. Here, all nuclei are treated classically (including the transferring hydrogen), and harmonic constraints are applied on the transferring hydrogen nucleus, the donor and acceptor atoms, and ligand centers, including the carbonyl carbons in the formate and formamide ligand groups and nitrogen atoms on the truncated amino ligands. These constraints are useful in our ADMP simulations because of the reduced active-site model considered here. In larger active-site models, these constraints are enforced indirectly by the protein active site. Furthermore, the center of the harmonic constraint on the transferring hydrogen is drawn toward the acceptor in a fashion similar to that highlighted in refs 54 and 62. The ADMP Hamiltonian is perturbed through the use of a set of harmonic constants to sample infrequent events such as transition barriers according to

$$H(\mathbf{R}, V, \mathbf{P}, W) = \frac{1}{2} Tr(V^{\mathrm{T}} \mathbf{M}^{-1} V) + \frac{1}{2} Tr(W \underline{\mu}^{-1/2} W \underline{\mu}^{-1/2}) +$$

$$E(\mathbf{R}, \mathbf{P}) + Tr[\mathbf{\Lambda}(\mathbf{P}\mathbf{P} - \mathbf{P})] + \sum_{i=1}^{N_C} \sum_{j=1}^{3} \frac{1}{2} k_{i,j} [\mathbf{R}_{i,j} - \mathbf{R}_{i,j}^0]^2 \quad (1)$$

where $\mathbf{R}$ and $V$ represent (in matrix notation) the classical nuclear positions and momenta with masses $\mathbf{M}$, respectively, and $\mathbf{P}$ and $W$ represent the electronic density matrix and its momenta, respectively, with fictitious inertia tensor[50] $\underline{\mu}$. The N-representability[50,57] of the density matrix is retained through the constraint term $Tr[\mathbf{\Lambda}(\mathbf{P}\mathbf{P} - \mathbf{P})]$, and additional harmonic constraints are enforced through the last term in the Hamiltonian above. The quantity $N_C$ represents the number of constrained atoms, and the quantity $k_{i,j}$ represents the harmonic constraint on the $j$th coordinate of the $i$th atom. Equations of motion are generated as outlined in ref 50 where first an ADMP Lagrangian is derived from a Legendre transform[50] of the ADMP Hamiltonian, followed by construction of Euler–Lagrange equations. The shared proton is dragged over the classical barrier by enforcing a constant velocity on the shared proton harmonic force center. The simulations are performed at constant temperature, which is enforced through velocity scaling as in previous ADMP studies.[40,63–69] The magnitude of the constraint potentials, characterized by the velocity and strength of the harmonic force constants are chosen to be in the order of 1000 pN/Å in directions perpendicular to the donor–acceptor direction as in previous studies[54,62] and 0 pN/Å (i.e., unconstrained) along the donor–acceptor direction. The donor carbon and transferring hydrogen are constrained in all three directions with similar constraints. A harmonic force constant of the order of 1000 pN/Å corresponds to a frequency of about 100 cm$^{-1}$ on the carbon, nitrogen, and oxygen atoms where the constraints are applied (estimated by using the fact that $k_{i,j} = m_i \omega_{ij}^2$ for the $j$th degree of freedom on the $i$th atom). Many simulations were
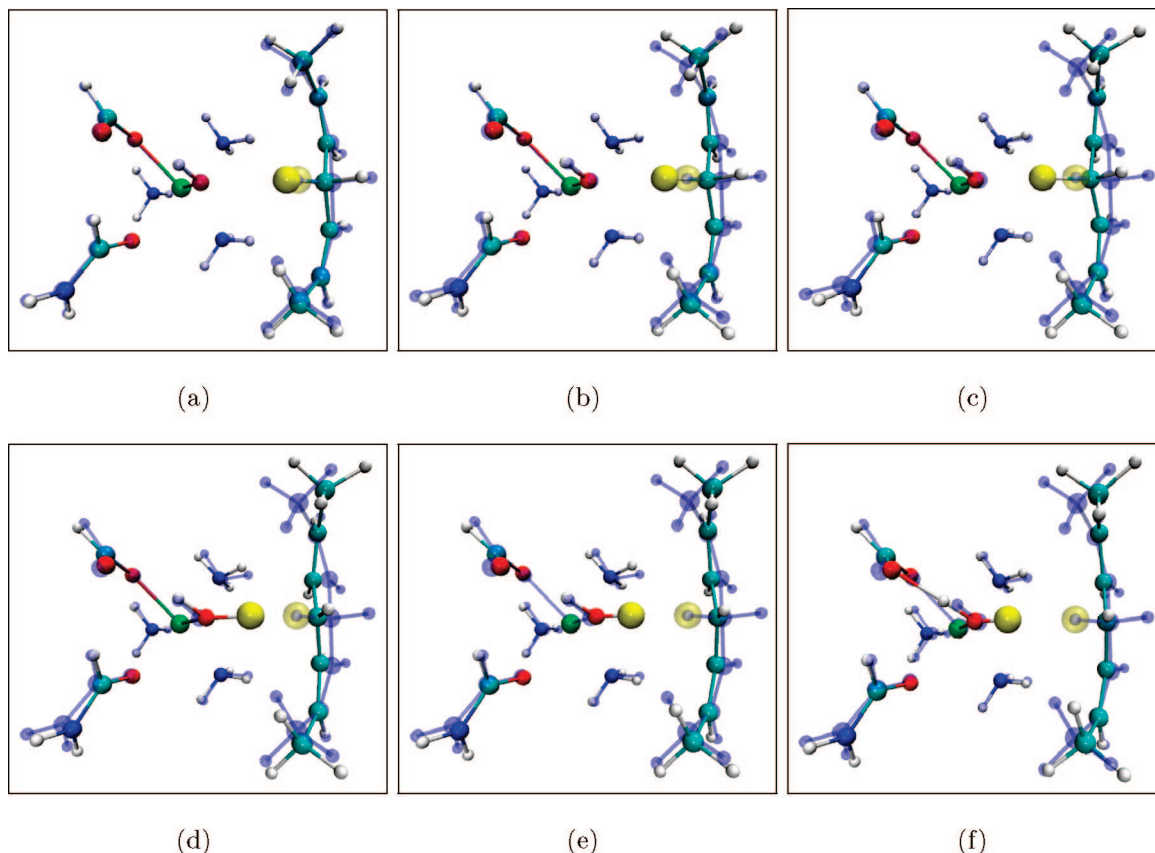
**Figure 4.** Snapshots from a constrained ADMP trajectory (eq 1) of structure I. In each panel, the transparent system represents the starting (reactant) geometry, and the opaque representation shows the molecular geometry at a later step along the ADMP trajectory. The opaque figures are arranged in increasing order of time, where panel (a) represents the early portion of the dynamics, and panel (f) represents the end of the constrained dynamics where the hydrogen-transfer process is complete. As the transferring proton (enlarged and highlighted in yellow) is pulled, the rest of the system simultaneously evolves. As seen in the last panel, once the hydrogen is transferred, the donor carbon correctly assumes an $sp^2$ geometry.

**TABLE 1: Summary of Proton Potential Surface for Quantum Dynamics and Eigenstate Evaluations**

| $(R_{CH} - R_{OH})/R_{CO}$ | $N_{Geom}{}^a$ | $N_{Grid}{}^b$ |
|---|---|---|
| $-0.413$ (reactant) | 1 | 408,321 |
| $-0.204$ to $-0.0586^c$ | 34 | 408,321 |
| $+0.412$ (product) | 1 | 408,321 |

[a] Represents the number of active-site geometries considered in the range given in column 1. [b] Represents the number of equally spaced proton coordinate grid points utilized to discretize the quantum wavepacket at each active-site geometry. [c] The classical transition state occurs in this range at $(R_{CH} - R_{OH})/R_{CO} = -0.0779$ as noted in Figure 3.

performed, where the constraint force constants are varied between simulations to reduce the level of perturbation on the system. A sample trajectory is depicted in Figure 4, where each panel shows both the starting geometry (transparent) and a geometry at a later point in the dynamics (opaque). By comparing the panels, one can see the hydrogen-transfer process, as well as the evolution of the rest of the system. Each simulation yields an approximation to a reaction path trajectory, which is refined through constrained local minimum geometry optimization calculations[55] similar to the ones described in the previous paragraph. Both techniques, ADMP and the relaxed-scan optimization discussed above, yield reaction profiles or minimum-energy paths that are practically indistinguishable and are shown in Figure 3. Furthermore, in all optimization calculations, all atoms are treated as classical point masses, and only the acceptor (oxygen)–transferring hydrogen distance is

constrained to sample the reaction coordinate. We again stress the fact that even though a simplified reaction coordinate variable is presented along the horizontal axis of Figure 3, all active-site atoms change coordinates along this minimum-energy path, which is also evident from Figure 4. Furthermore, the fact that many different ADMP simulations converge to the same reaction path shown in Figure 3 is not a surprise because of (a) the approximately one-dimensional nature of the classical hydrogen-transfer process (the dimensionality of the quantum hydrogen-transfer process will be discussed in the following sections) and (b) the size of the model system considered here.

**B. Determination of Hydrogen and Deuterium Nuclear Potential Surfaces for Quantum Dynamics along the Classical Path.** To account for nuclear quantization, we compute proton potential surfaces as a function of three-dimensional Cartesian proton coordinates for a large number of geometries along the reaction profile in Figure 3. In the discussion below, we refer to a proton potential-energy surface, but it is essentially a hydrogen nuclear potential surface. All electrons in the active-site model are treated together by using DFT and MP2. In Table 1, we provide a list of geometries or range of geometries (column 1) characterized by values of the simple reaction coordinate described in Figure 3, the number of geometries considered inside each range (column 2), and the number of proton coordinate grid points utilized to discretize the wavepacket for each active site geometry (column 3). The origin of the proton coordinate grid space is taken to be the center of the donor–acceptor axis. The three-dimensional Cartesian grid is
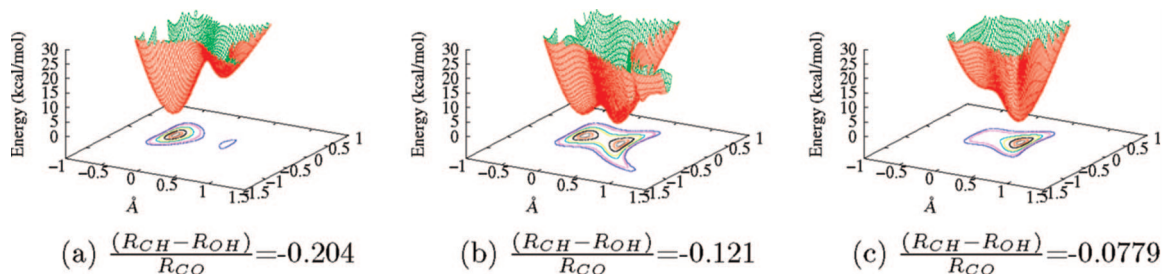
Hydrogen Tunneling in an Enzyme Active Site

*J. Phys. Chem. B, Vol. 112, No. 25, 2008* **7605**



$$\text{(a)} \quad \frac{(R_{CH}-R_{OH})}{R_{CO}}=-0.204 \qquad \text{(b)} \quad \frac{(R_{CH}-R_{OH})}{R_{CO}}=-0.121 \qquad \text{(c)} \quad \frac{(R_{CH}-R_{OH})}{R_{CO}}=-0.0779$$

**Figure 5.** Level surfaces as a function of two Cartesian dimensions and contour lines of the full proton potential-energy surface are provided at three points along the reaction coordinate. The origin is placed as described in the text. (a) Point on the reaction coordinate (see Figure 3) situated on the reactant side of the tunneling region. (b) Point in the tunneling region. (c) Surface at the classical transition state. It must be noted that the full proton potential energy surface utilized in the quantum dynamics is three-dimensional (that is, the potential depends on three Cartesian variables), and each figure here is a slice of the corresponding three-dimensional surface, provided here to display the reaction-coordinate dependence of the hydrogen nuclear potential. In all cases, the zero of potential has been shifted to correspond with the lowest-energy point. These curves have an important bearing on the results described in Section III.

oriented such that one axis is along the donor−acceptor line and a second axis is oriented along the plane comprising the donor carbon, the acceptor oxygen, and the hydrogen bonded to the donor carbon. The third axis is orthogonal to the plane comprising the other axes.

The electronic-structure calculations required for constructing the proton potential surface at each model system geometry were performed by using the B3LYP density functional and lanl2dz Gaussian-type basis set. The choice of functional and basis set was based on a comparison of the proton potential-energy surfaces and eigenstates obtained at different levels of theory including MP2. The benchmark data for DFT and MP2 are provided in the Appendix. It was found that the B3LYP density functional and lanl2dz basis provided acceptable accuracy at a limited computational expense. All calculations are performed by using a development version of the Gaussian series of electronic structure programs.[56] Furthermore, because of the large computational overhead involved in obtaining the full potential surface,[39,40] we enforced the following approximations. We first computed the proton potential surfaces for seven geometries in the range described in Table 1 by performing approximately 5000 B3LYP/lanl2dz electronic-structure calculations at each of the seven geometries. The energies obtained from these calculations were then interpolated to an extremely fine grid of over a million points via Hermite curve interpolation.[39,40,70–72] We then compared these potential surfaces to an approximate surface generated by (a) computing the energy, gradients, and Hessian for cases where the transferring hydrogen was donor-bound, acceptor-bound, and at the transition state for each of the seven geometries and (b) then constructing a smooth double-well potential by interpolating between two Harmonic curves centered on the donor and acceptor minima with curvatures determined from ab initio force constants. The interpolating function is a Gaussian parametrized to reproduce the ab initio barrier height. The full ab initio surfaces for the seven geometries described above were compared with the more approximate surface for a description of the localization properties of the low-lying eigenstates in all three directions. Because the comparisons were found to be adequate with good qualitative agreement, we chose to use the approximate surfaces for each geometry described in Table 1. (Note that the resultant proton coordinate potential surfaces are different for each geometry, and this aspect is further clarified in the discussion below.)

As seen from Table 1, the quantum potential surface of the tunneling proton is constructed on an extremely fine three-dimensional real space Cartesian grid. In Figure 5, we illustrate the proton potential surfaces encountered along the reaction coordinate. We present the potential surfaces as a function of

two Cartesian dimensions at different points along the reaction coordinate. The resultant quantum proton potentials have a smooth double-well character with minima on donor (reactant) and acceptor (product) sides. As one moves from reactant to product along the profile in Figure 3, the donor-side minimum increases in energy, and the acceptor-side minimum decreases in energy. Thus, the quantum mechanical hydrogen nucleus does not travel along the reaction coordinate in Figure 3 but scatters off time-dependent, three-dimensional double-well-type potentials (see Figure 5) that are created by the active-site geometry.

***Quantum Dynamics on the Hydrogen and Deuterium Nuclear Potential Surfaces.*** We construct the quantum dynamics of the hydrogen nucleus, represented as a wavepacket, on this reaction-coordinate-dependent potential where the quantum mechanical free propagator is approximated in the coordinate representation by using the distributed approximating functional (DAF) propagator.[38,48,49]

$$\widetilde{K}_k(x_i, x_j; t) = \frac{1}{\sigma(0)\sqrt{2\pi}} \left(\frac{-1}{\sqrt{2}\sigma(0)}\right)^k \exp\left(-\frac{(x_i-x_j)^2}{2\sigma(t)^2}\right) \times$$
$$\sum_{n=0}^{M/2} \left(\frac{\sigma(0)}{\sigma(t)}\right)^{2n+1} \left(\frac{-1}{4}\right)^n \frac{1}{n!} H_{2n+k}\left(\frac{x_i-x_j}{\sqrt{2}\sigma(t)}\right) \quad (2)$$

The terms $H_{2n+k}$ are Hermite polynomials, and $\sigma(t)^2 = \sigma(0)^2 + i\hbar t/m$.[38] Equation 2 represents a formally exact representation of the quantum dynamical free propagator[38,48,49] for $k = 0$ (see discussion below). The DAF propagator is also computationally efficient, because it is represented as a banded-sparse-Toeplitz matrix.[86] The quantum dynamical evolution of the wavepacket is constructed by using a Trotter symmetric factorization

$$\chi(x_i; t) = \sum_j \exp\left\{-\frac{iV(x_i; t)t}{2\hbar}\right\} \widetilde{K}_{k=0}(x_i, x_j; t) \times$$
$$\exp\left\{-\frac{iV(x_j; t)t}{2\hbar}\right\} \chi(x_j; 0) \quad (3)$$

and is utilized to compute the transmission coefficient of the wavepacket onto the product side as discussed in Section III.B. In eq 3, $\{x_i\}$ is the grid representation of the quantum proton, and $V(x_i)$ represents the hydrogen potential-energy surface described in Table 1 and illustrated in Figure 5. Furthermore, the hydrogen potential surfaces involved in our calculations have a confining effect. In other words, the reactant state proton potential tends to localize the lower-energy proton eigenstates to the donor side. The classical transition-state and product-state potential surfaces localize the lower-energy proton eigenstates to the acceptor side (see further discussion in regards to
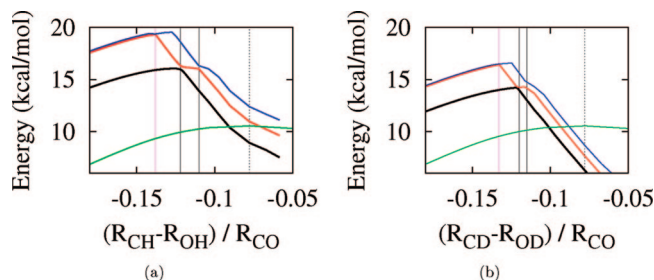
**Figure 6.** Figures (a) and (b) expand the view into the critical tunneling region described in Figure 3 and display the first few hydrogen (a) and deuterium (b) eigenstates. (The zero of energy is at the reactants, as in Figure 3.) These eigenstates drop below the reaction-path surface because the eigenstates close to the top of the barrier are localized on the product side. The classical transition state is shown by using a vertical dashed line, and curve crossings (see text) are represented by solid vertical lines. Critical symmetry driven curve crossings (vertical lines in magenta) and avoided crossing (solid vertical lines in black) are shown. These have a significant impact on the tunneling process.

the transition state in Section III.A), and intermediate-state surfaces enforce a double-well character that retains the proton to be partially bound to both donor and acceptor. As a result, the wavepacket is confined to the physical boundaries all through the dynamics, and no absorbing potentials[73–76] are necessary in our wavepacket dynamics calculations.

Although the evolution of the proton wavepacket is time-dependent, we also obtain instantaneous eigenstates of the quantum proton along the reaction coordinate. The functional form of these proton eigenstates and their respective time-dependent populations (computed from wavepacket propagation) allow us to understand the source of quantum tunneling in this problem and provide us with a deeper insight as discussed in Section III.A. Toward this, the quantum nuclear state is discretized in the coordinate representation, and the hydrogen (or deuterium) nuclear Hamiltonian is expressed by using the second derivative, zero-time limit of the distributed approximating functional propagator, (DAF), (eq 2)[38,48,49]

$$H(x_i, x_j) = -\frac{\hbar^2}{2m}\widetilde{K}_{k=2}(x_i, x_j; t = 0) + V(x_i)\delta_{x_i,x_j} \quad (4)$$

where $\tilde{K}_{k=2}(x_i, x_j; t = 0)$ is the second-derivative operator in the coordinate representation which is also obtained from eq 2. This representation, however, leads to an extremely large (million × million) matrix representation for the quantum proton Hamiltonian. We obtain the lowest 25 quantum eigenstates for all the geometries listed in Table 1 by using a very efficient Arnoldi iterative diagonalization procedure.[87] A discussion of the role of the quantum mechanical eigenstates on the tunneling mechanism is found in Section III.A.

## III. Results and Discussion

**A. Potential-Energy Surfaces and Quantum Nuclear Eigenstates of the Tunneling Hydrogen.** The evolution of the first three proton and deuteron eigenstates is depicted in Figure 6. Here, we also display the classical potential-energy surface from Figure 3, in green, and the classical transition-state barrier by using a dotted vertical line. In Figure 7, we provide a cross-section of the hydrogen potential surface with the active site at the classical transition-state geometry. Note that Figure 7 is essentially a contour plot and a one-dimensional projection of the curve already shown in Figure 5(c). In Figures 8 and 9, we provide an evolution of the three lowest hydrogen and deuterium nuclear eigenstates with key snapshots along the reaction coordinate. Several important features are apparent upon inspection of these figures.

First, the quantum nuclear eigenstate energies peak before the classical transition state as is apparent in Figure 6 and actually drop down as one approaches the classical barrier. This effect is completely caused by the quantum mechanical nature of the hydrogen nucleus and the associated potential-energy surface. As an illustration, we note in Figure 7 that the potential-energy minimum penetrates into the acceptor region at the classical transition-state geometry. We note further that although the classical transition-state geometry localizes the proton at the intersection of the two black crosswires in (Figure 7a), including nuclear quantization shifts the proton centroid position by about 0.5Å (to the red vertical line) as is clear upon inspection
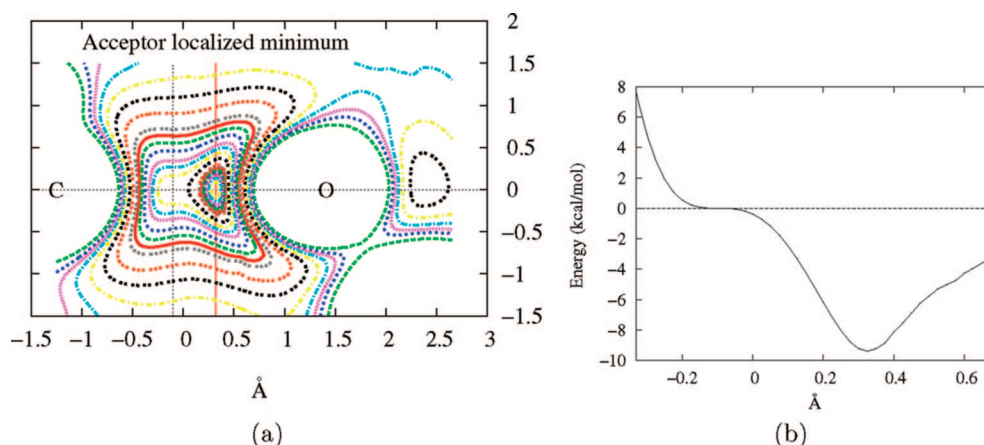


**Figure 7.** (a) Contour plot of the proton potential surface at the classical transition state geometry as a function of the Cartesian dimensions. This corresponds to one point ($(R_{CH} - R_{OH})/R_{CO} = -0.0779$) on the reaction coordinate in Figures 3 and 6. The average position of the proton ground state is marked with a red vertical line, and the state is relatively localized with standard deviations (0.075, 0.15, 0.12) Å along the three Cartesian dimensions, where the leading coordinate is along the donor–acceptor direction. The carbon (donor) and oxygen (acceptor) centers are shown, and the CO distance is 2.66 Å. Note that the classical transition-state geometry corresponds to a proton localized at the intersection of the two black horizontal and vertical lines. (b) Cut of the profile along the CO axis where the horizontal line at 0 kcal/mol marks the classical transition state. Again, it is clear that even though the classical geometry has the proton localized at 1.23Å from the donor carbon, the inclusion of nuclear quantum effects leads to a proton wave function with an average position about 0.5 Å away from the classical saddle point.
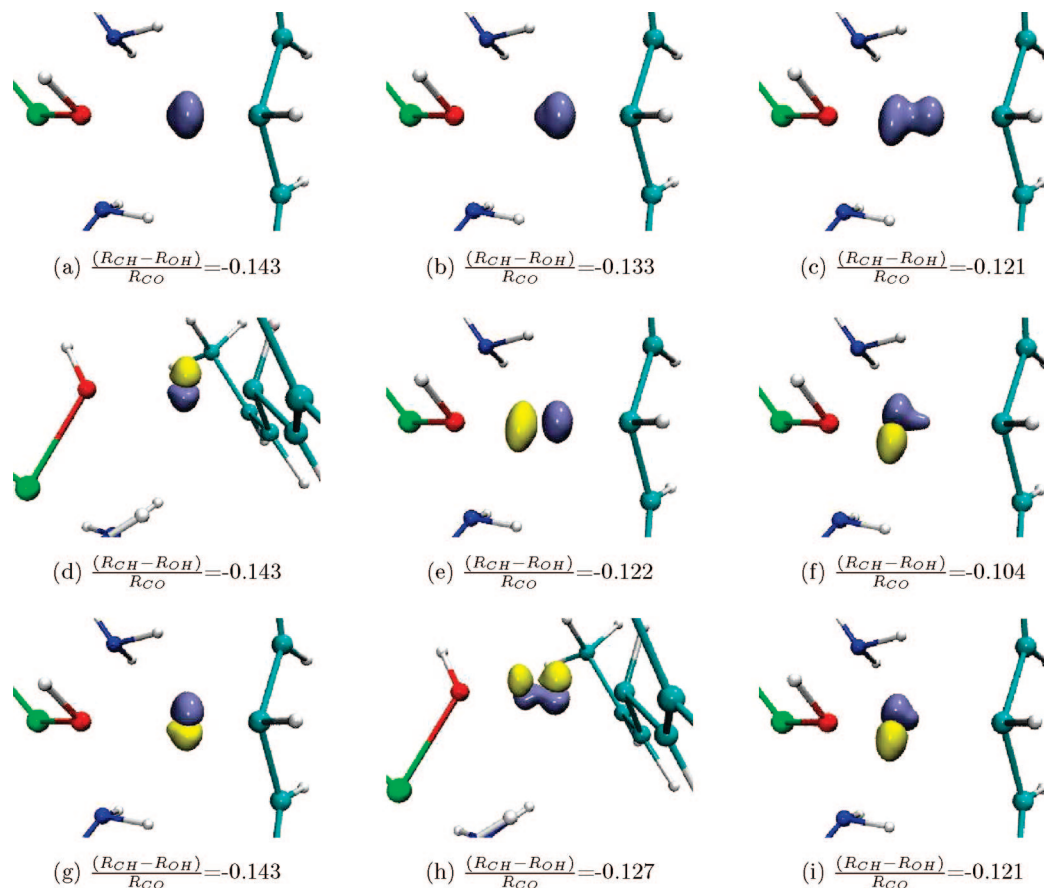
(a) $\frac{(R_{CH} - R_{OH})}{R_{CO}} = -0.143$    (b) $\frac{(R_{CH} - R_{OH})}{R_{CO}} = -0.133$    (c) $\frac{(R_{CH} - R_{OH})}{R_{CO}} = -0.121$

(d) $\frac{(R_{CH} - R_{OH})}{R_{CO}} = -0.143$    (e) $\frac{(R_{CH} - R_{OH})}{R_{CO}} = -0.122$    (f) $\frac{(R_{CH} - R_{OH})}{R_{CO}} = -0.104$

(g) $\frac{(R_{CH} - R_{OH})}{R_{CO}} = -0.143$    (h) $\frac{(R_{CH} - R_{OH})}{R_{CO}} = -0.127$    (i) $\frac{(R_{CH} - R_{OH})}{R_{CO}} = -0.121$

**Figure 8.** Evolution of the proton ground (a–c), first (d–f), and second (g–i) eigenstates. The phases of the orbitals are indicated by the yellow and ice-blue colors. Note that the orientation of panels (d) and (h) is slightly different from that of the rest owing to the rotated form of the orbitals.

of the potential surface depicted in Figure 7. As a result, the first few critical eigenstates of hydrogen and deuterium are localized on the acceptor side at the classical transition-state geometry. Furthermore, as noted in the caption of Figure 7, the ground eigenstate at the classical transition state geometry has a higher degree of relative delocalization perpendicular to the donor–acceptor direction, as compared to that along the donor–acceptor axis. As a result of these effects, the inclusion of nuclear quantization results in shifting the transition state toward the reactant, which is also consistent with the result in Figures 6(a) and 6(b). [Note the difference in horizontal axis between Figures 6(a) and 6(b) and 7. Figure 6(a) and 6(b) represents the change in electronic energy and nuclear eigenstate energy along the reduced reaction coordinate, $(R_{CH} - R_{OH})/R_{CO}$, whereas the horizontal axis in Figure 7 represents the quantum mechanical grid coordinate for the tunneling hydrogen nucleus.] In other words, if an effective reaction profile were to be constructed that included contributions from the quantum mechanical ground state of the tunneling nucleus (a zero-point corrected profile), the new profile would display a maximum closer to the reactant. It is important to note that this shift in the transition state is obtained here purely because of the quantization of the hydrogen nucleus and its associated potential surface. The precise location of the shifted transition state, however, depends on the populations of each hydrogen and deuterium eigenstate during dynamics, because each of the eigenstates peaks at different values of the reaction coordinate. (See Figures 6(a) and 6(b)). Furthermore, a comparison of Figure 6, panels (a) and (b), shows that the eigenstates of hydrogen and deuterium peak at different values. Hence, it is foreseeable

that the quantum dynamically corrected transition states for hydrogen and deuterium are at different points along the reaction coordinate and are temperature-dependent. However, one advantage of our approach is that we do not need to make an effort to determine this special point on the surface for reasons that will become apparent in Section III.B. (For reference, we provide the shape of the lowest hydrogen eigenstate at its maximum point in Figure 10.) Similar shifts in the classical transition state have been noted for other systems by using variational transition-state theory,[22] through maximizing the classical overbarrier reactive flux. Here, however, the effect is obtained by considering the quantum nuclear eigenstates. This aspect receives further attention at the end of this section.

Second, we note the presence of curve crossings and avoided crossings for the first three proton and deuteron eigenstates displayed in Figures 6(a) and 6(b) by using solid vertical lines. (These crossings are also seen for higher energy levels.) The presence of these intersection points has an effect on the dynamics of hydrogen transfer that is quite similar to the presence of such intersections in electronic dynamics; that is, the quantum dynamical hydrogen-transfer process in the vicinity of these crossings is governed by nonadiabatic population transfer to excited states. Indeed, as we note in the next section, our quantum dynamical treatment is vibrationally nonadiabatic because it involves the time evolution of the nuclear wavepacket and hence captures such population-transfer effects. In addition, it is clear from these figures that the curve crossings have greater proximity along the reaction coordinate, that is, occur much more rapidly for deuterium as compared to hydrogen, because of smaller gaps between the eigenstates of deuterium.
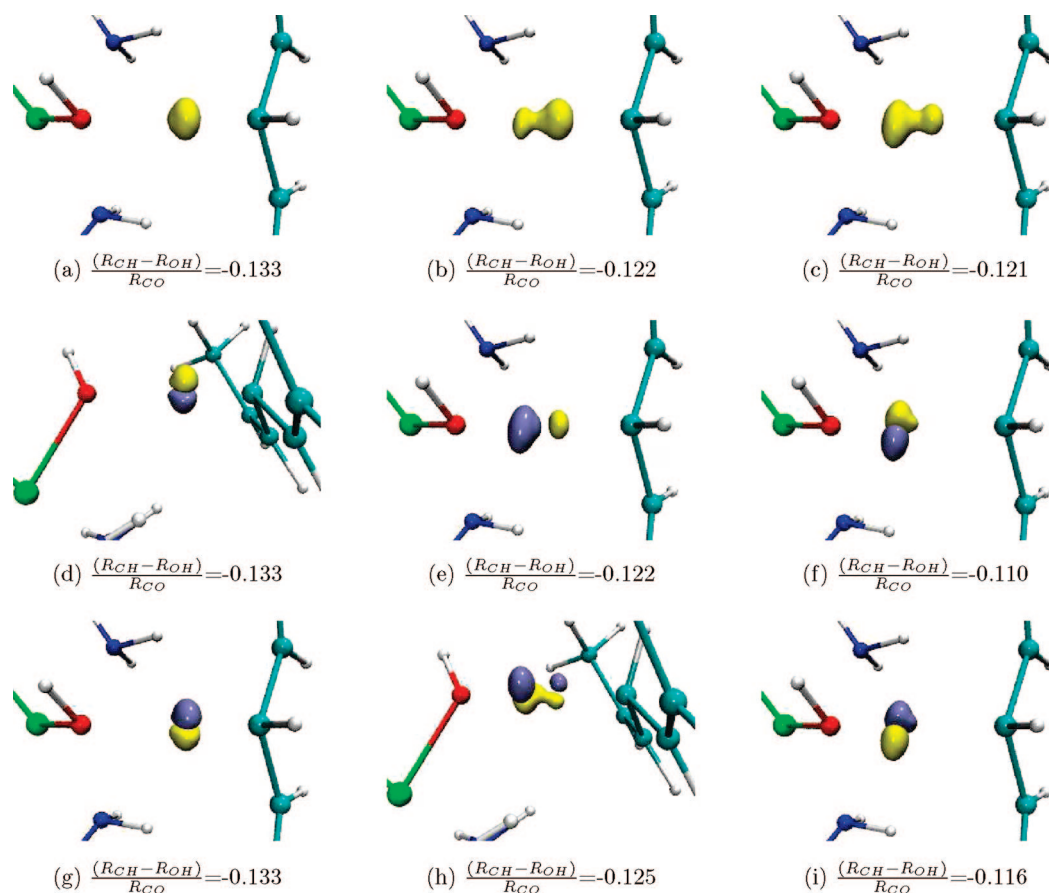
**Figure 9.** Evolution of the deuteron ground (a–c), first (d–f), and second (g–i) eigenstates. The phases of the orbitals are indicated by the yellow and ice-blue colors. Note that the orientation of panels (d) and (h) is slightly different from that of the rest owing to the rotated form of the orbitals. Note further that the chosen slices for deuterium are closer to the transition state (with respect to the hydrogen figures in Figure 8) because the advent of tunneling for deuterium follows that in hydrogen. The deuteron orbitals are more localized than the proton orbitals in Figure 8.

Finally, the nature of quantum potential surface and the avoided crossings have a critical effect on the evolution of the nuclear eigenstates and govern the hydrogen/deuterium tunneling processes. The eigenstates that are harmonic-like in the reactant (or donor) channel start to gradually sample the acceptor side of the potential as one traverses along the reaction profile in Figure 3, and anharmonicity contributions start to grow. As is clear from Figures 8 and 9, the ground eigenstates smoothly tunnel from the donor to acceptor sides; the transition from a spherical s-type proton orbital on the reactant channel to a distorted s-type proton orbital with two lobes, indicative of a population transfer, is clearly noted in these figures, for both hydrogen and deuterium. [The distorted s-type orbitals may also be rationalized within an s−p hybrid orbital picture, where the s and p orbitals are (a) distorted because of anharmonicity and (b) mix with unequal coefficients. See discussion below.] It is further important to note that the anharmonicity of the quantum potential surface plays a critical role in these distorted s-type proton orbitals, which are significant for the tunneling process. The key features of the quantum dynamical potential surface that impact this process are as follows. Closer to the donor channel, the potential is harmonic-like in all three directions as is clear from the s-like ground state in Figures 8(a) and 9(a). However, the potential is more confining along the donor−acceptor line, which lowers the energy of the excited p-type proton eigenstates along the orthogonal directions ($p_\perp$). See Figures 8(d) and 8(g) for proton and Figures 9(d), and 9(g) for deuteron, where eigenstates perpendicular to the donor−acceptor line are presented. Along the reaction profile, the proton potential surface acquires a partial double-well character, and the potential cut

along the donor−acceptor line begins to relax in confinement. This relaxation stabilizes the p-type function along the donor−acceptor axis ($p_\parallel$) and subsequently reduces its energy to that below the other two $p_\perp$ eigenstates (Figure 8(e) for hydrogen and Figure 9(e) for deuterium). In Figures 6(a) and 6(b), this happens around the first curve crossing (splitting point of the red and blue curves), which is a true crossing based on the orthogonal symmetries of the interacting $p_\parallel$ and $p_\perp$ orbitals. The red curve, after the branching, acquires a $p_\parallel$ character. At the second avoided crossing, the ground and first excited states acquire bonding (distorted s) and antibonding ($p_\parallel$) linear combinations. The ground state acquires density across the barrier as well as on the donor and acceptor wells, whereas the first excited state has density on both wells, with a node in the middle. It is interesting to note that both of these functions have a probability density that promotes tunneling. Another important feature that is seen upon inspection of Figures 8(g)−(i) and 9(g)−(i) is that the $p_\perp$ orbitals are directly passed to the acceptor side through an intervening, twisted $\pi$-bond orbital (Figures 8(h) and 9(h)). An antibonding $\pi$-type interaction is also seen higher in energy, for the fourth eigenstate, but is not shown here.

Based on the above discussion, it is important to note that a situation that retains population on the proton ground state leads to tunneling through a distorted s-type function that cuts right through the barrier. On the contrary, a situation with increased proton excited eigenstate participation leads to an increasing transfer probability not only through $p_\parallel$ states but also through $p_\perp$ states which, in a semiclassical sense, amounts to tunneling around the minimum-energy path. In all cases, the proton orbitals have significant population orthogonal to the donor−acceptor
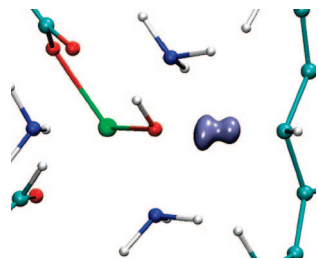
Hydrogen Tunneling in an Enzyme Active Site

*J. Phys. Chem. B, Vol. 112, No. 25, 2008* **7609**



**Figure 10.** Ground eigenstate for proton at the maximum zero-point corrected energy point, $(R_{CH} - R_{OH})/R_{CO} = -0.121$ (see Figure 6).
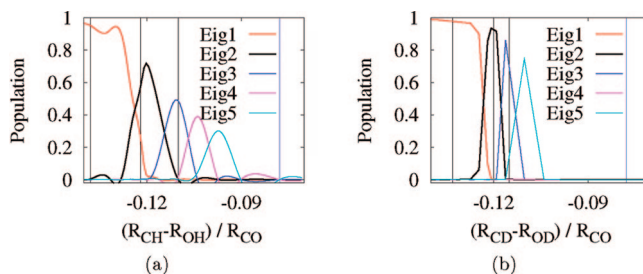


**Figure 11.** Instantaneous wavepacket components along the time-dependent eigenstates for proton (a) and deuteron (b). Nuclear excited-state contributions are critical in both cases. The classical transition state is represented by using the solid blue vertical line, and the avoided crossings between eigenstates 2−3, 1−2, and 2−3 are reproduced here from Figures 6(a) and 6(b) with the black solid vertical lines.

axis, an aspect of the tunneling phenomenon which a one-dimensional analysis fails to capture. It must be further noted that the significance of excited nuclear wave functions has previously been observed by other investigators[12,79] by using a one-dimensional model potential to describe the shared hydrogen. In our case, we see contributions from excited $p_{||}$-type states to the tunneling process which can be captured in one-dimensional approximations. However, as is clear from the discussion above, we also note contributions from $p_{\perp}$-type states to the tunneling process which obviously cannot be envisioned through one-dimensional model potentials.

We must also note that our computations are restricted to the model described in Figure 2. Hence, the fundamental assumption in these calculations is that the quantum dynamical evolution of the shared proton is local and mostly governed by the potential surface as enforced by the neighboring atoms. In this regard, we must note that Klinman and co-workers have recorded an important dependence of the KIE on mutations. These mutations are not included in the reduced active-site model dealt with here, and hence, our current calculations are not sensitive to these studies. We are currently extending our quantum wavepacket AIMD method to include QM/MM and continuum solvent models, which will allow us to treat these problems in the future.

Additionally, for reasons that become apparent in the next section, we have chosen not to identify the special point where the quantum mechanically corrected potential surface has a maximum value along the reaction coordinate. However, the physical factors that govern the position of such a point include the proximity of the curve crossings and the gap between the quantized levels, both of which affect the population of excited states. These factors are qualitatively different from those utilized in semiclassical models based on transition-state theory to determine the surface of maximum forward flux.

**B. Quantum Dynamical Wavepacket Propagation of the Tunneling Hydrogen.** Although the previous subsection does provide important physical insight into the transfer process, it must be noted that computation of the proton eigenstates is not a requirement in our dynamical algorithm. We directly propagate the initial wavepacket on potential surfaces that depend on the geometry of the active site. Toward this, the time-dependent evolution of the quantum nuclear system is constructed through Trotter symmetric factorization (eq 3), and the free propagator, $\tilde{K}_{k=0}(x_i, x_j; t)$, is approximated by using eq 2.[38,48,49] The initial wavepacket is constructed as a Boltzmann average of proton and deuteron eigenstates computed with the active-site geometry at the reactant configuration. The propagation is carried out by using eq 3, and the scheme is vibrationally nonadiabatic because it involves the time evolution of the nuclear wavepacket. In this sense, our approach is related to other non-traditional methods used to study condensed-phase hydrogen transfer.[80] The nonadiabatic nature of the quantum dynamics of the tunneling

proton forms a critical basis for our analysis as we project the instantaneous wavepacket onto the proton eigenstate representations discussed in the previous section. In Figure 11, we present the evolution of projections of the quantum wavepacket onto the respective proton and deuteron eigenstates as a function of reaction coordinate. It is clear that many eigenstates contribute to the nonadiabatic tunneling process, including all those discussed in the previous section. The population transfers occur right before the curve crossings noted in Figure 6(a) and 6(b), as is to be expected. Because these curve crossings occur more rapidly for deuterium than for hydrogen (on account of the smaller gaps between eigenstates in deuterium), the population transfers also occur more rapidly for deuterium. By extension, close to the classical transition state, the excited-state populations in deuterium are much higher than those in hydrogen. Hence, the positions of the avoided crossings constitute an important difference between the behavior of hydrogen and deuterium transfer.

It is also critical to note that the $p_{\perp}$ orbitals in Figures 8(d) and 8(g) and 9(d) and 9(g) are, in fact, populated in Figures 11. Therefore, population transfer along directions orthogonal to the donor−acceptor axis has a significant contribution. The fact that vibrational excitations occur close to the transition state during a reactive process is already well-known from classical transition-state theory and is the hallmark of many semiclassical theories. Here, however, the vibrational excitations occur before the classical transition state because of nuclear quantization of the transferring atom, the proximity of curve crossings, and the smaller gap between the quantized states in the case of deuterium.

To further quantify the tunneling process, we conduct an analysis of the total probability density of the time-dependent wavepacket on the product-bound side of the proton potential-energy surface at each time step. In other words, we compute the transmission coefficient ($T_H$ and $T_D$) of the wavepacket as shown in Figure 12. As can be seen, the transmission coefficients for both hydrogen and deuterium are significant even before the classical transition state is reached, indicating tunneling in both cases. It is further interesting to note that the transmission coefficient for hydrogen, in Figure 12, starts to become important at the intersection point between the ground and first excited state at which point the first excited state (the p state in Figure 8(d)−(e)) assumes a significant population. The deuterium transmission coefficient, on the contrary, begins to assume significant proportions only when the second and higher level excited states are populated ($(R_{CH} - R_{OH})/R_{CO} > -0.12$ in Figures 12 and 11(b)) on account of the lower delocalization of the associated eigenstates.
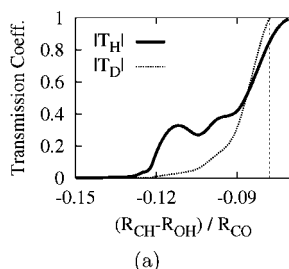
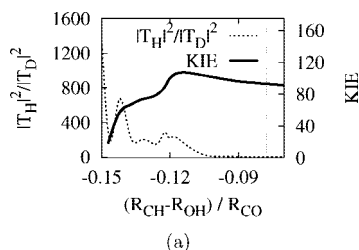**Figure 12.** Transmission coefficients for hydrogen and deuterium.



**Figure 13.** Evolution of eq 5.

The ratio of transmission probabilities $|T_H|^2/|T_D|^2$ in Figure 13 is initially large because for small values of $|T_H|$ and $|T_D|$, that is, far from the classical transition state, the transmission amplitude for hydrogen is significantly greater than that for deuterium on account of the larger de Broglie wavelength of hydrogen. However, closer to the classical transition state, the active-site geometry starts to achieve a conformation that favorably places the hydrogen and deuterium atoms on the product side of the proton potential (see Figure 7), and both transmission coefficients become comparable. The unidirectional running average of the quantity $|T_H|^2/|T_D|^2$

$$\left\langle \frac{|T_H|^2}{|T_D|^2} \right\rangle = \frac{1}{\int^{R_C} dR_{RC}} \left[ \int^{R_C} dR_{RC} \frac{|T_H|^2}{|T_D|^2} \right] \quad (5)$$

is the average ratio of transmission probabilities as one approaches the top of the barrier. Its evolution is displayed by using the solid curve in Figure 13. Here, $R_{RC} = (R_{CH} - R_{OH})/R_{CO}$. As can be seen, the running average converges to a value in the range 80−100, with an average value of 88, which is in good agreement with the experimentally observed KIE.[13]

The running average ratio defined in eq 5 has the following properties. As stated earlier, it is constructed from transmission coefficients of hydrogen and deuterium, and hence, each term in the summation in the numerator on the right side corresponds to the cumulated ratio of probabilities of finding one particle over another on the product side for each point on the reaction coordinate. The numerator is a constrained ensemble average of $|T_H|^2/|T_D|^2$, where the configurations for the ensemble are chosen to be along the minimum-energy classical path and the ensemble average is constructed for $|T_H|^2/|T_D|^2$ from each of the chosen configurations. This explains the notation used on the left-hand side of eq 5, where the ensemble average is performed on the reaction coordinate. It is further important to note that the transmission probability is directly related to the probability flux in the direction of the product[18] and is hence connected to the flux correlation functions utilized in ref 12 to compute the KIE. In addition, because the transmission amplitude represents the probability of hydrogen and deuterium transfer, it is inversely related to the survival amplitude of the wavepacket in the reactant channel. Furthermore, the survival probability is related to the flux operator formalism that has

been used by many investigators[33] in quantum dynamics. Finally, the populations in the product state obtained by using the transmission coefficients is also related to the method of computing quantum classical rates.[82]

## IV. Conclusions

We have studied the hydrogen tunneling process in a model system that represents the active site of Soybean Lipoxygenase-1. First, an approximation to a minimum-energy path is obtained from AIMD simulations followed by a sequence of electronic-structure optimization and frequency calculations. Proton potential-energy surfaces are then computed at many points along the minimum energy path through density functional calculations. Quantum dynamics calculations are performed on these dynamical potential-energy surfaces, and the KIE is computed through a constrained ensemble average of the proton wavepacket transmission coefficient ratios. The quantum dynamics for the proton is performed by using a formally exact form of the discretized quantum propagator.

On the basis of studies on our model system, we reproduce the experimentally observed KIE for SLO-1. We also provide unique physical insights into the nature of the tunneling mechanism. By computing proton eigenstates and eigenenergies along the reaction path, we note that the nature of the quantum dynamical potential surface, the proton and deuteron eigenstates, and associated curve crossings and avoided crossings have an important role on the tunneling process. Specifically, we show that when the ground-state proton orbitals are considered, tunneling occurs parallel to the reaction coordinate (along the donor−acceptor axis) via a distorted s-type (bonding) orbital. However, as higher states become populated in the dynamics, tunneling also simultaneously occurs through p-type antibonding proton eigenstates parallel to the reaction coordinate (and hence referred to as $p_\parallel$) as well as through p-type eigenstates directed orthogonally ($p_\perp$) to the reaction coordinate. For instance, for the second excited state, the transfer happens via $\pi$-type proton orbital interactions which are created from the bonding overlap of two polarized proton states, one positioned near the donor site and the other close to the acceptor site. From the time-dependent evolution of the quantum wavepacket, we show that there is significant population of the higher-energy eigenstates. The significance of excited nuclear wave functions has also been observed by other investigators[12,79] through one-dimensional model potentials. Whereas $p_\parallel$-type states can be inferred from one-dimensional potentials, the contributions from $p_\perp$-type states to the tunneling process cannot be envisioned through a one-dimensional model. Furthermore, the population transfer between the proton eigenstates occurs near avoided crossings and curve crossings, which are present in abundance. The curve crossings occur on the basis of the symmetry of interacting p-type proton orbitals, whereas the avoided crossings, as usual, occur through bonding and antibonding linear combinations of near degenerate proton eigenstates. Because the intersection points occur more rapidly for deuterium than for hydrogen, excited-state populations for deuterium are higher than for hydrogen. Although these results pertain to the model described in Figure 2, we are currently extending our quantum wavepacket AIMD method to include QM/MM and continuum solvent models which will allow us to treat a larger portion of the enzyme in the future.

Additionally, our calculations show that a quantum dynamically corrected transition state may be shifted toward the reactants relative to the classical transition state. However, the location of this special point on the surface would be temperature-dependent, such

Hydrogen Tunneling in an Enzyme Active Site

*J. Phys. Chem. B, Vol. 112, No. 25, 2008* **7611**

**TABLE 2: Comparison of Structures I and II**

| $(R_{CH} - R_{OH})/R_{CO}$ (structure I) | $(R_{CH} - R_{OH})/R_{CO}$ (structure II) | $1/N\|R_I - R_{II}\|_2$[a] (Å) | $E_{II} - E_I$ (kcal/mol) |
|---|---|---|---|
| −0.41 (reactant) | −0.40 (reactant) | 0.019 | 0 |
| −0.29 | −0.29 | 0.017 | −0.291 |
| −0.26 | −0.25 | 0.017 | 0.362 |
| −0.24 | −0.23 | 0.018 | 0.0571 |
| −0.20 | −0.20 | 0.017 | −0.656 |
| −0.18 | −0.18 | 0.017 | −0.430 |
| −0.15 | −0.15 | 0.016 | −0.578 |
| −0.13 | −0.13 | 0.015 | −0.298 |
| −0.11 | −0.11 | 0.014 | −0.0576 |
| −0.078 (TS) | −0.062 (TS) | 0.016 | 0.826 |
| 0.41 (product) | 0.44 (product) | 0.028 | −1.42 |

[a] Represents the $L^2$-norm $[\|\cdots\|_2]$ of the difference in the distance matrix for structures I and II divided by the number of elements in the distance matrix. Only distance matrix elements shared between the structures are used for this comparison

dependence arising from the precise populations of the respective proton eigenstates, and will also in general be different for proton and deuteron transfer. We make no attempt to find this special point because quantum mechanical tunneling occurs over a wide area, and the KIE is computed from the transmission coefficients calculated over a wide area along the reaction coordinate. We further emphasize that the shift in the corrected transition state is obtained here purely from quantizing the transferred proton. At the classical transition state, the modes orthogonal to the donor−acceptor axis are less restricted than the modes parallel to the reaction coordinate, as indicated by the confinement induced by the quantum potential surface in the respective directions. As a result of the lower degree of confinement along directions orthogonal to the donor−acceptor axis, barrier recrossing effects may be estimated to be small. But the quantum mechanically corrected transition state is shifted toward reactants purely because of the structure of the eigenstates in the tunneling region and associated curve intersections.

**Appendix. Comparison of Structures I and II and Estimation of Accuracy of the Proton Potential Surface from DFT and MP2 Calculations**

In this section, we provide some benchmark studies to probe the effect of using structure I in our simulations as opposed to structure II. We further examine the computational error caused by the use of density functional theory to model the proton quantum dynamical surface in comparison with MP2.

By comparing the reaction profiles for structures I and II (see Figure 2 for a description of structures I and II), we examine the limitations on the energetics of ligand binding caused by employing the truncated representation of histidine in structure I. First, a large number of geometries for both structures were obtained corresponding to reaction coordinate values ranging from the reactant to classical transition state, including many different geometries in the critical tunneling region. These geometries were obtained through constrained optimization techniques. In addition, we also examined the product complex for both model structures. The results for a sample set spanning the tunneling region, the reactant, product, and classical transition-state complexes along the reaction profile are displayed in Table 2. (The errors for all other geometries studied are of a

**TABLE 3: Comparison of the MP2 and B3LYP Potential Energy Surfaces**

| $(R_{CH} - R_{OH})/R_{CO}$ | $\Delta\rho_\beta$[a] | $\Delta V_1$[b] | $\Delta V_2$ | $\Delta V_3$ |
|---|---|---|---|---|
| −0.201 | $1.93 \times 10^{-3}$ | 0.0579 | 0.256 | 0.882 |
| −0.197 | $2.04 \times 10^{-3}$ | 0.0645 | 0.269 | 0.951 |
| −0.190 | $2.36 \times 10^{-3}$ | 0.0877 | 0.303 | 1.16 |
| −0.176 | $2.85 \times 10^{-3}$ | 0.0954 | 0.385 | 1.98 |
| −0.160 | $3.69 \times 10^{-3}$ | 0.125 | 0.540 | 3.49 |
| −0.143 | $5.47 \times 10^{-3}$ | 0.166 | 0.935 | 3.35 |
| −0.122 | $9.01 \times 10^{-3}$ | 0.226 | 1.91 | 1.72 |

[a] Error in a Boltzmanized wavepacket at 300K. See eq A1.
[b] Error in kcal/mol as described in eq A2.

magnitude similar to those presented in Table 2.) The first two columns in the table compare the reaction coordinates values in structures I and II. These values present a study of the local geometry around the tunneling hydrogen, involving the donor and acceptor atoms. A more complete analysis of the Cartesian coordinates for all common atoms involved in the models studied is presented in the third column of the table by way of the average error in the shared elements of the distance matrices. The fourth column compares the electronic-structure (B3LYP/lanl2dz) energies at each point. We note that the local geometries are similar, and the average deviation in energy is about 0.498 kcal/mol through the reaction profile. In addition, average deviation in geometry between the structures is ∼0.019 Å. Clearly, there is reasonable agreement between the reaction energetics and geometric parameters provided by the two models which provides a justification for using the smaller model structure in the extensive quantum dynamics simulations presented here. We also note that similar reduced models have been utilized by other investigators in studying metalloenzymes,[15,51] and these have been found to provide good qualitative description of the reaction energetics.

To gauge the restrictions imposed by the use of density functional theory in computing the proton quantum dynamical potential surface, we also benchmarked the B3LYP/lanl2dz calculations with MP2/lanl2dz calculations by comparing properties of one-dimensional proton potential-energy surfaces encountered by the shared proton along the donor−acceptor line for structure I. Several geometries in the critical tunneling region were considered, and the nature of the potential surface was inspected. All geometries considered were originally obtained from B3LYP/lanl2dz constrained optimization. The proton potential-energy surfaces were then obtained by using B3LYP and MP2. Our comparison involved intrinsic properties of the potential surface, namely, the eigenstates, as well as direct comparisons of the surfaces. Our results are displayed in Table 3. In column I, we present the reaction coordinate. In the second column, we compare the MP2 and B3LYP thermally sampled hydrogen wavepackets by using

$$\Delta\rho_\beta = \frac{1}{\sqrt{N_{Grid}}}\sqrt{\int d\vec{x}[\rho_\beta^{MP2}(\vec{x}) - \rho_\beta^{DFT}(\vec{x})]^2} \quad (A1)$$

where $\rho_\beta^{MP2}(\vec{x})[\equiv|\chi_\beta^{MP2}(\vec{x})|^2]$ and $\rho_\beta^{DFT}(\vec{x})[\equiv|\chi_\beta^{DFT}(\vec{x})|^2]$ are the thermally sampled wavepacket densities obtained from

$$\chi_\beta^{MP2}(\vec{x}) = \sum_i e^{-\beta E_i^{MP2}}\chi_i^{MP2}(\vec{x})$$

$$\chi_\beta^{DFT}(\vec{x}) = \sum_i e^{-\beta E_i^{DFT}}\chi_i^{DFT}(\vec{x})$$

and $N_{Grid}$ is the number of grid points used to discretize the wave function. The hydrogen eigenfunctions, $\chi_i^{MP2}(\vec{x})$ and $\chi_i^{DFT}(\vec{x})$ were calculated by using ab initio potential-energy surfaces and

the kinetic-energy operator in eq 4. (The last paragraph in Section II describes the diagonalization procedure.) Here, $\beta$ represents the inverse temperature computed at 300K. Equation A1 represents the root-mean-square deviation of the individual wavepacket densities along the grid. Because the eigenstate shapes play an important role in the tunneling process, this comparison reveals insights into how the tunneling mechanism may differ for B3LYP surfaces compared to MP2 surfaces.

The last three columns in Table 3 compare the potential-energy surfaces weighted by using the ground, first, and second excited eigenstate probability densities

$$\Delta V_i = \sqrt{\int d\vec{x} \left[ V^{\mathrm{MP2}}(\vec{x})\rho_i^{\mathrm{MP2}}(\vec{x}) - V^{\mathrm{DFT}}(\vec{x})\rho_i^{\mathrm{DFT}}(\vec{x}) \right]^2} \quad (\mathrm{A2})$$

where $\rho_i^{\mathrm{DFT}}(\vec{x}) = |\chi_i^{\mathrm{DFT}}(\vec{x})|^2$ and similarly for MP2. Equation A2 is essentially a grid-by-grid comparison of the functions that form the expectation value of the potential in DFT and MP2. For these calculations, the minimum energy for all surfaces was set to zero. This measure shows how the energies of the potentials differ in the critical (wavepacket-populated) regions. We utilize the first three eigenstates here because they are most significant in the critical tunneling region noted in Figure 6(a). The comparisons based on the eigenstates and the potentials indicate that the agreement between the B3LYP and MP2 surfaces are generally acceptable in regions populated by the lower eigenstates, but the two electronic-structure methods begin to differ as higher-energy eigenstates contribute. These issues will be considered in further detail as part of future publications.

## References and Notes

(1) Isaacs, N. *Physical Organic Chemistry*; Wiley & Sons: New York, 1995.

(2) Nagel, Z.; Klinman, J. *Chem. Rev.* **2006**, *106* (8), 3095–3118.

(3) Hammes-Schiffer, S.; Benkovic, S. J. *Annu. Rev. Biochem.* **2006**, *75*, 519.

(4) Benkovic, S. J.; Hammes-Schiffer, S. *Science* **2006**, *312*, 208.

(5) Bahnson, B. J.; Colby, T. D.; Chin, J. K.; Goldstein, B. M.; Klinman, J. P. *Proc. Natl. Acad. Sci. U.S.A.* **1997**, *94*, 12797.

(6) Garcia-Viloca, M.; Gao, J.; Karplus, M.; Truhlar, D. G. *Science* **2004**, *303*, 5655.

(7) Olsson, M. H. M.; Siegbahn, P. E. M.; Warshel, A. *J. Am. Chem. Soc.* **2004**, *126*, 2820–2828.

(8) Antoniou, D.; Basner, J.; Nunez, S.; Schwartz, S. *Chem. Rev.* **2006**, *106* (8), 3170–3187.

(9) Klinman, J. P. *Pure Appl. Chem.* **2003**, *75*, 601.

(10) Liang, Z. X.; Klinman, J. P. *Curr. Opin. Struct. Biol.* **2004**, *14*, 648.

(11) Pu, J. Z.; Gao, J. L.; Truhlar, D. G. *Chem. Rev.* **2006**, *106*, 3140–3169.

(12) Hatcher, E.; Soudackov, A. V.; Hammes-Schiffer, S. *J. Am. Chem. Soc.* **2007**, *129*, 187.

(13) Glickman, M. H.; Wiseman, J. S.; Klinman, J. P. *J. Am. Chem. Soc.* **1994**, *116*, 793–794.

(14) Antoniou, D.; Schwartz, S. D. *Proc. Natl. Acad. Sci. U.S.A.* **1997**, 9412360–12365.

(15) Lehnert, N.; Solomon, E. I. *J. Biol. Inorg. Chem.* **2003**, *8*, 294.

(16) Hatcher, E.; Soudackov, A. V.; Hammes-Schiffer, S. *J. Am. Chem. Soc.* **2004**, *126*, 5763–5775.

(17) Olsson, M. H. M.; Siegbahn, P. E. M.; Warshel, A. *J. Biol. Inorg. Chem.* **2004**, *9*, 96–99.

(18) Siebrand, W.; Smedarchina, Z. *J. Phys. Chem. B* **2004**, *108*, 4185.

(19) Segraves, E. N.; Holman, T. R. *Biochemistry* **2003**, *42*, 5236–5243.

(20) Jonsson, T.; Glickman, M. H.; Sun, S. J.; Klinman, J. P. *J. Am. Chem. Soc.* **1996**, *118*, 10319–10320.

(21) Alhambra, C.; Corchado, J.; Sanchez, M. L.; Garcia-Viloca, M.; Gao, J.; Truhlar, D. G. *J. Phys. Chem. B* **2001**, *105*, 11326–11340.

(22) Garcia-Viloca, M.; Alhambra, C.; Truhlar, D. G.; Gao, J. L. *J. Comp. Chem.* **2003**, *24*, 177–190.

(23) Gao, J. *Acc. Chem. Res.* **1996**, *29*, 298.

(24) Hammes-Schiffer, S. *Curr. Opin. Struct. Biol.* **2004**, *14*, 192–201.

(25) Warshel, A.; Weiss, R. M. *J. Am. Chem. Soc.* **1980**, *102*, 6218.

(26) Chang, Y.-T.; Miller, W. H. *J. Phys. Chem.* **1990**, *94*, 5884.

(27) Day, T. J. F.; Soudachov, A. V.; Cuma, M.; Schmidt, U. W.; Voth, G. A. *J. Chem. Phys.* **2002**, *117*, 5839–5849.

(28) Wang, F.; Voth, G. A. *J. Chem. Phys.* **2005**, *122*, 144105.

(29) Billeter, S. R.; Webb, S. P.; Agarwal, P. K.; Iordanov, T.; Hammes-Schiffer, S. *J. Am. Chem. Soc.* **2001**, *123*, 11262–11272.

(30) Warshel, A.; Sharma, P.; Kato, M.; Xiang, Y.; Liu, H.; Olsson, M. *Chem. Rev.* **2006**, *106* (8), 3210–3235.

(31) Cao, J.; Voth, G. A. *J. Chem. Phys.* **1994**, *101*, 6168.

(32) Jang, S.; Voth, G. A. *J.Chem. Phys.* **1999**, *111*, 2371.

(33) Miller, W. H.; Schwartz, S. D.; Tromp, J. W. *J. Chem. Phys.* **1983**, *79*, 4889.

(34) Kuznetsov, A. M.; Ulstrup, J. *Can. J. Chem.* **1999**, *77*, 1085.

(35) Bolhuis, P. G.; Dellago, C.; Chandler, D.; Geissler, P. *Annu. Rev. Phys. Chem.* **2002**, *59*, 291.

(36) Dellago, C.; Bolhuis, P. G.; Csajka, F. S.; Chandler, D. *J. Chem. Phys.* **1998**, *108* (5), 1964–1977.

(37) Iyengar, S. S.; Jakowski, J. *J. Chem. Phys.* **2005**, *122*, 114105.

(38) Iyengar, S. S. *Theo. Chem. Acc.* **2006**, *116*, 326.

(39) Jakowski, J.; Sumner, I.; Iyengar, S. S. *J. Chem. Theory Comput.* **2006**, *2*, 1203–1219.

(40) Sumner, I.; Iyengar, S. S. *J. Phys. Chem. A* **2007**, *111*, 10313–10324.

(41) Glickman, M. H.; Wiseman, J. S.; Klinman, J. P. *J. Am. Chem. Soc.* **1994**, *116*, 793.

(42) Jonsson, T.; Glickman, M. H.; Sun, S. J.; Klinman, J. P. *J. Am. Chem. Soc.* **1996**, *118*, 10319.

(43) Rickert, K. W.; Klinman, J. P. *Biochemistry* **1999**, *38*, 12218.

(44) Knapp, M. J.; Rickert, K.; Klinman, J. P. *J. Am. Chem. Soc.* **2002**, *124*, 3865.

(45) Meyer, M. P.; Klinman, J. P. *Chem. Phys.* **2005**, *319*, 283.

(46) Samuelsson, B.; Dahlen, S. E.; Lindgren, J. A.; Rouzer, C. A.; Serhan, C. N. *Science* **1987**, *237*, 1171–1176.

(47) Ghosh, J.; Myers, C. E. *Proc. Natl. Acad. Sci. U.S.A.* **1998**, *95*, 13182–13187.

(48) Hoffman, D. K.; Nayar, N.; Sharafeddin, O. A.; Kouri, D. J. *J. Phys. Chem* **1991**, *95*, 8299.

(49) Kouri, D. J.; Huang, Y.; Hoffman, D. K. *Phys. Rev. Lett.* **1995**, *75*, 49–52.

(50) Iyengar, S. S.; Schlegel, H. B.; Millam, J. M.; Voth, G. A.; Scuseria, G. E.; Frisch, M. J. *J. Chem. Phys.* **2001**, *115*, 10291.

(51) Blomberg, M.; Siegbahn, P. *J. Phys. Chem. B* **2001**, *105* (39), 9375–9386.

(52) Voter, A. F. *J. Chem. Phys.* **1997**, *106*, 4665.

(53) Voter, A. F. *Phys. Rev. Lett.* **1997**, *78*, 3908.

(54) Park, S.; Khalili-Araghi, F.; Tajkhorshid, E.; Schulten, K. *J. Chem. Phys.* **2003**, *119*, 3559–3566.

(55) Hratchian, H.; Schlegel, H. B. *Finding minima, transition states, and following reaction pathways on ab intio potential energy surfaces*; Elsevier: Amsterdam, 2005; p 195.

(56) Frisch, M. J.; Trucks, G. W.; Schlegel, H. B.; Scuseria, G. E.; Robb, M. A.; Cheeseman, J. R.; Montgomery, J. A., Jr.; Vreven, T.; Kudin, K. N.; Burant, J. C.; Millam, J. M.; Iyengar, S. S.; Tomasi, J.; Barone, V.; Mennucci, B.; Cossi, M.; Scalmani, G.; Rega, N.; Petersson, G. A.; Nakatsuji, H.; Hada, M.; Ehara, M.; Toyota, K.; Fukuda, R.; Hasegawa, J.; Ishida, M.; Nakajima, T.; Honda, Y.; Kitao, O.; Nakai, H.; Klene, M.; Li, X.; Knox, J. E.; Hratchian, H. P.; Cross, J. B.; Bakken, V.; Adamo, C.; Jaramillo, J.; Gomperts, R.; Stratmann, R. E.; Yazyev, O.; Austin, A. J.; Cammi, R.; Pomelli, C.; Ochterski, J. W.; Ayala, P. Y.; Morokuma, K.; Voth, G. A.; Salvador, P.; Dannenberg, J. J.; Zakrzewski, V. G.; Dapprich, S.; Daniels, A. D.; Strain, M. C.; Farkas, O.; Malick, D. K.; Rabuck, A. D.; Raghavachari, K.; Foresman, J. B.; Ortiz, J. V.; Cui, Q.; Baboul, A. G.; Clifford, S.; Cioslowski, J.; Stefanov, B. B.; Liu, G.; Liashenko, A.; Piskorz, P.; Komaromi, I.; Martin, R. L.; Fox, D. J.; Keith, T.; Al-Laham, M. A.; Peng, C. Y.; Nanayakkara, A.; Challacombe, M.; Gill, P. M. W.; Johnson, B.; Chen, W.; Wong, M. W.; Gonzalez, C.; Pople, J. A. *Gaussian 03*, revision B.01; Gaussian, Inc.: Wallingford, CT, 2004.

(57) Schlegel, H. B.; Millam, J. M.; Iyengar, S. S.; Voth, G. A.; Daniels, A. D.; Scuseria, G. E.; Frisch, M. J. *J. Chem. Phys.* **2001**, *114*, 9758.

(58) Schlegel, H. B.; Iyengar, S. S.; Li, X.; Millam, J. M.; Voth, G. A.; Scuseria, G. E.; Frisch, M. J. *J. Chem. Phys.* **2002**, *117*, 8694.

(59) Iyengar, S. S.; Schlegel, H. B.; Voth, G. A.; Millam, J. M.; Scuseria, G. E.; Frisch, M. J. *Israel J. Chem.* **2002**, *42*, 191–202.

(60) Iyengar, S. S.; Frisch, M. J. *J. Chem. Phys.* **2004**, *121*, 5061.

(61) Rega, N.; Iyengar, S. S.; Voth, G. A.; Schlegel, H. B.; Vreven, T.; Frisch, M. J. *J. Phys. Chem. B* **2004**, *108*, 4210–4220.

(62) Ilan, B.; Tajkhorshid, E.; Schulten, K.; Voth, G. A. *Proteins: Struct., Funct., Bioinf.* **2004**, *55*, 223–228.

(63) Iyengar, S. S. *J. Chem. Phys.* **2007**, *126*, 216101.

(64) Iyengar, S. S.; Petersen, M. K.; Day, T. J. F.; Burnham, C. J.; Teige, V. E.; Voth, G. A. *J. Chem. Phys.* **2005**, *123*, 084309.

(65) Iyengar, S. S.; Day, T. J. F.; Voth, G. A. *Int. J. Mass Spectrom.* **2005**, *241*, 197–204.

(66) Iyengar, S. S. *J. Chem. Phys.* **2005**, *123*, 084310.

(67) Li, X.; Teige, V. E.; Iyengar, S. S. *J. Phys. Chem. A* **2007**, *111*, 4815–4820.

Hydrogen Tunneling in an Enzyme Active Site

*J. Phys. Chem. B, Vol. 112, No. 25, 2008* **7613**

(68) Li, X.; Moore, D. T.; Iyengar, S. S. *J. Chem. Phys.* **2008**, *128*, 184308.

(69) Iyengar, S. S.; Li, X.; Sumner, I. *Adv. Quantum Chem.* **2007**, in press.

(70) Carter, S.; Bowman, J. M.; Braams, B. *J. Chem. Phys. Lett.* **2001**, *342*, 636–642.

(71) Christoffel, K. M.; Bowman, J. M.; Braams, B. J. *J. Chem. Phys.* **2001**, *115*, 11021–11024.

(72) Bartels, R. H.; Beatty, J. C.; Barsky, B. A. *An Introduction to Splines for use in computer graphics and geometric modeling*; Morgan Kaufman Publishers, Inc.: Los Altos, CA, 1987.

(73) Leforestier, C.; Wyatt, R. E. *J. Chem. Phys.* **1983**, *78*, 2334–2344.

(74) Neuhasuer, D.; Baer, M. *J. Chem. Phys.* **1989**, *90*, 4351–4355.

(75) Iyengar, S. S.; Kouri, D. J.; Hoffman, D. K. *Theor. Chem. Acc.* **2000**, *104*, 471.

(76) Althorpe, S. C. *J. Chem. Phys.* **2001**, *114*, 1601–1616.

(77) Althorpe, S. C.; Kouri, D. J.; Hoffman, D. K. *J. Chem. Phys.* **1997**, *107*, 7816–7824.

(78) Peng, T.; Zhang, J. Z. H. *J. Chem. Phys.* **1996**, *105*, 6072–6074.

(79) Meyer, M. P.; Klinman, J. P. *Chem. Phys.* **2005**, *319*, 283–296.

(80) Kiefer, P. M.; Hynes, J. T. *J. Phys. Chem. A* **2004**, *108*, 11793.

(81) Shankar, R. *Principles of Quantum Mechanics*; Springer: New York, 1994.

(82) Hammes-Schiffer, S.; Tully, J. *J. Chem. Phys.* **1994**, *101*, 4657–4667.

(83) Sorensen, D. C. *SIAM J. Matrix. Anal. Appl.* **1992**, *13*, 357–385.

(84) Golub, G. H.; van Loan C. F., *Matrix Computations*; The Johns Hopkins University Press: Baltimore, 1996.

(85) Parlett, B. N.; Saad, Y. *Lin. Alg. Appl.* **1987**, *88/89*, 575–595.

(86) The $(i,j)$th element of a Toeplitz matrix depends only on $|i-j|$. This property of the free propagator in eq 2 yields an efficient scheme where only the first (banded and sparse) row of the matrix representation of the time-evolution operator needs to be stored.

(87) The Arnoldi diagonalization works as follows.[39,83–85] First. a random initial vector depicting the proton quantum state is obtained, and the sequential action of the Hamiltonian on this starting vector is computed to obtain a family of basis vectors $\{\eta_i\}_{i=0,..,M}$ where $M$ is of the order of 100 (much smaller than the size of the Hamiltonian matrix). The family of basis vectors $\{\eta_i\}_{i=0,..,M}$ form a Krylov[84] basis. The Hamiltonian is then projected onto the Krylov basis to obtain a smaller $M \times M$ matrix which can be diagonalized easily to obtain the first few eigenstates of the proton.